

Coronal magnetic field modeling using stereoscopy constraints

I. Chifu^{1,2,3}, B. Inhester¹, and T. Wiegelmann¹

¹ Max-Planck Institute for Solar System Research, 37077 Göttingen, Germany
e-mail: chi.fu@mps.mpg.de

² Astronomical Institute of Romanian Academy, 040557 Bucharest, Romania

³ Technical University Braunschweig, 38106 Braunschweig, Germany

Received 27 August 2013 / Accepted 26 February 2015

ABSTRACT

Aims. Nonlinear force-free field (NLFFF) extrapolation has been used extensively in the past to extrapolate solar surface magnetograms to stationary coronal field models. In theoretical tests with known boundary conditions, the nonlinear boundary value problem can be solved reliably. However, if the magnetogram is measured with errors, the extrapolation often yields field lines that disagree with the shapes of simultaneously observed and stereoscopically reconstructed coronal loops. We here propose an extension to an NLFFF extrapolation scheme that remedies this deficiency in that it incorporates the loop information in the extrapolation procedure. **Methods.** We extended the variational formulation of the NLFFF optimization code by an additional term that monitors and minimizes the difference of the local magnetic field direction and the orientation of 3D plasma loops. We tested the performance of the new code with a previously reported semi-analytical force-free solution.

Results. We demonstrate that there is a range of force-free and divergence-free solutions that comply with the boundary measurements within some error bound. With our new approach we can obtain the solution out of this set the coronal fields which is well aligned with given loops.

Conclusions. We conclude that the shape of coronal loops reconstructed by stereoscopy may lead to an important stabilization of coronal NLFFF field solutions when, as is typically the case, magnetic surface measurements with limited precision do not allow determining the solution solely from photospheric field measurements.

Key words. Sun: magnetic fields – Sun: corona

1. Introduction

The importance of the magnetic field in the corona has been recognized decades ago. Still, we cannot reliably determine sufficient details, for example, in the distribution of the electric current, which are required to predict the onset of eruptions and other dynamic processes, except in perhaps a few singular events.

The magnetic field in the corona has occasionally been measured directly. Polarization measurements of the green corona line Fe XIV in principle indicate the field orientation in the plane of the sky (House et al. 1982; Arnaud 1992). In a few cases, successful attempts have also been made to measure the Zeeman splitting of infrared lines (Lin et al. 2000). However, these observations do not provide the coronal field directly but need to be elaborately inverted since they integrate along the line of sight through the optically thin corona.

Instead, an indirect approach has been widely pursued in the past. It makes use of standard magnetic field measurements in the photosphere. For several years, these observations from various observatories and spacecraft provide the full magnetic field vector. These data are extrapolated into the corona by means of solving a nonlinear boundary value problem based on the assumption of a force-free coronal field (NLFFF) extrapolation. Different and competing numerical procedures are in use to solve the NLFFF extrapolation problem. Many of these procedures easily solve this problem correctly if consistent boundary data are given with sufficient accuracy

(Schrijver et al. 2006; Inhester & Wiegelmann 2006). This also produced convincing results in individual applications to observed data (see Wiegelmann & Sakurai 2012, and references therein for an overview).

However, when the procedures are applied to real data, it is difficult to estimate the extrapolation error quantitatively. A test that has been applied in the past is to compare field lines from the extrapolation model with the shape of simultaneously observed extreme-ultraviolet (EUV) loops. These loops are assumed to be firmly aligned along the magnetic field. For instance, Carcedo et al. (2003) have proposed a quantitative norm to measure the distance between projected field lines and 2D loop structures in EUV images. They used a linear force-free field approach and fitted alpha by comparing the field model with the coronal images. Given a single-loop image, this comparison is often inconclusive because the height of the loop is only poorly determined from a single projection. In an extensive study, various NLFFF extrapolations of the same magnetogram data set have been compared with 3D loop shapes reconstructed from two EUV images by stereoscopy (De Rosa et al. 2009). All field models obtained agreed with the boundary data within reasonable error, but none produced field lines that were well aligned with the loops reconstructed from stereoscopy. The typical angular discrepancy between the local loop orientation and the model field direction was about 20 deg. Even though the study suffered from the fact that the reconstructed loops were not well located above the magnetogram area that supplied the boundary condition for the extrapolation, the study

shed some light on the difficulty of reconstructing the coronal magnetic field from observations: measurement errors as they are probably unavoidable in magnetograms can easily degrade the quality of the extrapolation result, especially at higher altitudes above the solar surface. [Wiegelmann & Neukirch \(2002\)](#) have optimized the α parameter of a linear force-free field such that the best agreement between the model field line and a 3D loop obtained from stereoscopy was achieved. [Aschwanden et al. \(2012\)](#), [Aschwanden \(2013\)](#) and [Aschwanden & Malanushenko \(2013\)](#) used a perturbed potential field in order to improve the match between model field lines and given 3D loops.

In addition to the measurement uncertainties, there are other sources of potential errors in the NLFFF boundary data ([Régnier 2013](#)). The field observations on the surface do not yield a unique orientation of the transverse field component (180°-ambiguity, [Metcalf et al. 2006](#); [Leka et al. 2009](#)). Moreover, a more or less stationary coronal magnetic field is necessary. Since in the low- β plasma of the corona the Lorentz force formally dominates, stationarity insures that the Lorentz term is small and the magnetic field force-free. The plasma β , however, is not necessarily small in the height range between the photosphere, where the field measurements are made, and the base of the corona ([Metcalf et al. 1995](#); [Moon et al. 2002](#)).

Stereoscopy of coronal loops also has typical deficiencies. EUV loops can often only be discerned near active regions and must be identified uniquely in two or more simultaneous images. Reconstructing them by stereoscopy is also prone to some typical errors. These are basically of geometrical origin and occur when the viewing angle between the two stereo projections is small or near 180 deg, or where the loop tangent tends to become orthogonal to the epipolar plane that defines the local reconstruction geometry ([Inhester 2006](#); [Aschwanden 2011](#)).

We therefore prefer not to consider extrapolation and loop stereoscopy as competing methods for determining the coronal magnetic field. We instead aim to combine independent observations of photospheric magnetic field and loop stereoscopy to construct a magnetic field model that complies with both observations.

In our view, it would be desirable to build the field model from the set of NLFF fields. In this paper we propose and test a coronal field reconstruction method that combines a conventional NLFFF extrapolation method with the 3D data from individual loops. We assume that the loops were obtained from stereoscopic reconstruction beforehand. Among the extrapolation algorithms in use, the variational approach appears the most convenient to include the loop data. In the following section we describe our approach, in Sect. 3 it is tested using boundary values and simulated loops from a known force-free field. The robustness of our results is demonstrated by testing the realistic situations when both the loop and the magnetogram data are perturbed from their consistent values.

2. Extension of the NLFFF optimization scheme

As mentioned in the introduction, we basically extend the NLFFF variational method such that in addition to the boundary data, loop data from a stereoscopic reconstruction, for instance, are also taken care of. The variational method has originally been proposed by [Wheatland et al. \(2000\)](#) and was extended by [Wiegelmann \(2004\)](#) and [Tadesse et al. \(2011\)](#). The essential approach is to minimize a scalar cost function L_{tot} that consists of a number of terms L_n quantifying constraints that the final solution should satisfy. As a rule, these terms are convex, positive definite integrals of coronal field functionals. In the most

recent version of the NLFFF variational method ([Wiegelmann & Inhester 2010](#)), these terms are

$$L_1 = \frac{1}{V} \int_V w_f \frac{|(\nabla \times \mathbf{B}) \times \mathbf{B}|^2}{B^2} d^3r \quad (1)$$

$$L_2 = \frac{1}{V} \int_V w_f |\nabla \cdot \mathbf{B}|^2 d^3r \quad (2)$$

$$L_3 = \frac{1}{S} \int_S (\mathbf{B} - \mathbf{B}_{\text{obs}}) \cdot \text{diag}(\sigma_q^{-2}) \cdot (\mathbf{B} - \mathbf{B}_{\text{obs}}) d^2r. \quad (3)$$

Here, \mathbf{B}_{obs} is the observed field on the photospheric boundary surface S , and $\sigma_q(\mathbf{r})$ are estimated measurement errors for the three field components $q = x, y, z$ on S (see [Wiegelmann & Inhester 2010](#), for more details). In L_1 and L_2 , w_f is a boundary weight function that allows keeping the other boundary values of the computational box V unmodified during the optimization (see [Wiegelmann 2004](#), for more details).

To these terms, we add a new one that constrains the magnetic field to be aligned to selected loops that are obtained, for example, from a 3D stereoscopic reconstruction. We represent them by 3D functions $c_i(s)$ where the loop parameter s is scaled to the geometrical length along the loop and index i identifies different loops. The term has the form

$$L_4 = \sum_i \frac{1}{\int_{c_i} ds} \int_{c_i} \frac{|\mathbf{B} \times \mathbf{t}_i|^2}{\sigma_{c_i}^2} ds \quad (4)$$

where $\mathbf{t}_i = \frac{d\mathbf{c}_i}{ds}$.

Here, $\mathbf{t}_i(s)$ is the tangent vector along the i th loop and has unit length due to the scaling of the loop parameter s .

Just as the boundary data above, the loop reconstruction may also include errors. These depend on the stereoscopic view geometry and may well vary along the loop. Typically, they are largest at the top of the loop where the tangent vector \mathbf{t}_i becomes orthogonal to the normal of the epipolar plane that defines the local stereoscopic geometry. To take these errors into account, we include a function $\sigma_{c_i}(s)$ that is a relative measure of the estimated error of the tangent direction $\mathbf{t}_i(s)$ along the loop i . In the test calculations below, we choose known loops as test data and consequently set $\sigma_{c_i}(s)$ to unity. We term this extended version of our extrapolation scheme the S-NLFFF variational problem, where S stands for stereoscopy.

For practical calculations, the magnetic field, its boundary data, and the loop data are given on discrete grids. The respective discretized cost function contributions are named \mathcal{L}_i . For the magnetic field and photospheric boundary data we use a regular, equidistant Cartesian grid with nodes \mathbf{r}_k (here, k is a 3D multi-index for the grid indices along the three axes). A complication with the new term \mathcal{L}_4 arises because it does not share the common equidistant grid of the field and boundary data. If we discretize the loop parameter s equidistantly by $s \rightarrow s_j = j\Delta s$, the new variational term becomes

$$\mathcal{L}_4 = \sum_i \frac{1}{\sum_j \Delta s} \sum_j \frac{|\overline{\mathbf{B}}(\mathbf{c}_i(s_j)) \times \mathbf{t}_i(s_j)|^2}{\sigma_{c_i}^2(s_j)} \Delta s \quad (5)$$

where $\overline{\mathbf{B}}(\mathbf{r})$ is the field interpolated from neighboring grid points \mathbf{r}_k onto a position \mathbf{r} and $\sigma_{c_i}^2(s_j)$ is the variance of the tangent vector $\mathbf{t}_i(s_j)$. Here again, i enumerates the loop, s_j is the discretized distance parameter along the loop and k is the multi-index of the Cartesian grid. The discretization distance Δs along

the loops was chosen to be the fraction 1/5 of the Cartesian grid spacing. To this end, we minimize

$$\mathcal{L}_{\text{tot}} = \sum_{n=1,4} \xi_n \mathcal{L}_n \quad (6)$$

where the ξ_i are regularization weights attached to each term \mathcal{L}_n . Their role and how they are determined is explained below.

To perform the minimization, we need the functional derivatives of the discretized \mathcal{L}_i with respect to the field components $\mathbf{B}(\mathbf{r}_k)$. For the conventional terms, \mathcal{L}_n , $n = 1, 2, 3$ these derivatives have been calculated in [Wiegelmann \(2004\)](#) and [Wiegelmann & Inhester \(2010\)](#). For the new term we find

$$\begin{aligned} F_{4,q}(\mathbf{r}_k) &= \frac{\partial \mathcal{L}_4}{\partial B_q(\mathbf{r}_k)} \\ &= \sum_i \frac{2}{\sum_j \Delta s} \sum_j \frac{d\mathbf{F}_{c_i}(s)}{\sigma_{c_i}^2(s_j)} \cdot \frac{\partial \bar{\mathbf{B}}(\mathbf{c}_i(s_j))}{\partial B_q(\mathbf{r}_k)} \Delta s \end{aligned} \quad (7)$$

where $d\mathbf{F}_{c_i}(s) = \bar{\mathbf{B}}(\mathbf{c}_i(s)) - (\bar{\mathbf{B}}(\mathbf{c}_i(s)) \cdot \mathbf{t}_i(s))\mathbf{t}_i(s)$

for all three spatial components q and all grid points k . Note that $d\mathbf{F}_{c_i}$ is the projection of the local $\bar{\mathbf{B}}$ normal to the loop tangent. For a linear interpolation in the regular Cartesian grid we use here, $\partial \bar{\mathbf{B}}/\partial B_q(\mathbf{r}_k)$ is just the interpolation weight of field component $B_q(\mathbf{r}_k)$ in $\bar{\mathbf{B}}(\mathbf{c}_i(s_j))$. This weight is nonzero only if the loop point $\mathbf{c}_i(s_j)$ is located in a grid box for which \mathbf{r}_k is one of its corners.

Similar vectors \mathbf{F}_n for the terms $n = 1, 2, 3$ in Eqs. (1)–(3) have been calculated for the NLFFF optimization method by [Wiegelmann \(2004\)](#). The minimization of \mathcal{L}_{tot} is then performed by a Landweber iteration

$$\mathbf{B} \leftarrow \mathbf{B} - \mu \sum_{n=1}^4 \xi_n \mathbf{F}_n \quad (8)$$

This iteration reduces \mathcal{L}_{tot} at each iteration step, provided, μ is small enough. If \mathcal{L}_{tot} at iteration n is larger than at iteration $n+1$, then our code automatically reduces the step size μ by a factor of 2. Otherwise, the value for μ is enhanced by a factor of 1.01. The iteration is stopped if μ is reduced below a threshold value, here set to 10^{-7} .

For consistent boundary and loop data, all the terms (1), (2) (3) and (4) in the continuous equivalent of the cost function (6) could theoretically be reduced to zero if the provided boundary data \mathbf{B}_{obs} are consistent. However, for the equivalent discretized problem, the terms \mathcal{L}_n in (6) usually cannot all vanish simultaneously because most often an exact discrete solution of the variational problem does not exist. Additionally, if the boundary and loop data were measured they are likely to include observational errors that most probably render the measurements inconsistent. The best we can hope for in this situation is to minimize \mathcal{L}_{tot} to a value low enough for that the respective discrete solution of the magnetic field to be an acceptable approximation to the real field \mathbf{B} . We call $\mathcal{L}_{\text{tot}}^\infty$ and \mathcal{L}_i^∞ , $i = 1, \dots, 4$ the residual values of the cost function and its decomposition at the end of the iteration. Note that due to the introduction of \mathcal{L}_3 , our formulation of the NLFFF problem is not overdetermined anymore because the derivatives $\partial \mathcal{L}_{\text{tot}}/\partial B_q(\mathbf{r}_k)$ provide just the correct number of equations for each unknown field component $B_q(\mathbf{r}_k)$. Instead, the difficulty is now shifted to the possibility that the minimum $\mathcal{L}_{\text{tot}}^\infty$ is finite if the magnetogram data \mathbf{B}_{obs} are inconsistent. Moreover, the Hessian $\partial^2 \mathcal{L}_{\text{tot}}/\partial B_q(\mathbf{r}_k) \partial B'_q(\mathbf{r}'_k)$ at the minimum might have

a wide range of eigenvalues so that the minimization is poorly conditioned.

With $\mathcal{L}_i^\infty > 0$, the weights ξ_i in \mathcal{L}_{tot} play an important role because they determine how the residual value of $\mathcal{L}_{\text{tot}}^\infty$ is distributed among the individual terms \mathcal{L}_i^∞ . In general, the residual value of a single \mathcal{L}_i^∞ can be reduced to much lower values if ξ_i is enhanced with respect to the other ξ_j , $j \neq i$. However, the respective \mathcal{L}_j^∞ will then increase depending on how much the constraints represented by the discretized terms \mathcal{L}_i and \mathcal{L}_j are in conflict. This way, each of the \mathcal{L}_i^∞ can be considered a function of the whole set of weights $\{\xi_1, \dots, \xi_4\}$ through the minimization process. The goal, of course, is to choose these weights such that all \mathcal{L}_i^∞ are reduced to their lowest possible value.

Typically, the \mathcal{L}_i^∞ cannot be decreased to zero but are bounded below by a discretization-noise or data-noise level. In a $\log \mathcal{L}_i^\infty$ vs. $\log \mathcal{L}_j^\infty$ representation, the solutions for different ξ_i and ξ_j are then located on an L-shaped curve with the two legs defining the two noise levels. The best solution is then located in the corner of the L-curve ([Hansen 2010](#)), and it then minimizes $\log \mathcal{L}_i^\infty + \log \mathcal{L}_j^\infty$. Generalized to several regularization terms, the best choice of ξ_1, \dots, ξ_4 is obtained if $\sum_i \log \mathcal{L}_i^\infty(\xi_1, \dots, \xi_4)$ is minimal.

There are, however, additional considerations. For example, if σ_q and σ_c introduced in Eqs. (3) and (4) represent realistic error estimates, we might wish to tune the residual value of these terms to about unity. With these values, the extrapolated field complies with the observations to the order of the observational errors. With any further reduction of \mathcal{L}_3 and \mathcal{L}_4 , we would try to adjust the field $\mathbf{B}(\mathbf{r}_k)$ to the data noise at the expense of minimizing its divergence and Lorentz force.

3. Testing the method

We tested our extended optimization method, S-NLFFF by recovering the semi-analytical force-free field solution proposed by [Low & Lou \(1990\)](#) from various simulated input data. The set of solutions of Low & Lou has been used by many authors to perform field tests of NLFFF solutions ([Schrijver et al. 2006](#); [Amari et al. 2006](#); [Valori et al. 2007](#); [Wiegelmann & Inhester 2010](#); [Thalmann et al. 2011](#)). The field model Low & Lou has a spherical harmonic angular dependence about a virtual center. The dependence on radial distance from this center is obtained from the solution of a nonlinear Sturm-Liouville eigenvalue problem. In our and similar tests, the center of the solution is placed below the bottom surface of the computational box and, to break the symmetry of the spherical harmonic, its axis is tilted obliquely with respect to the edges of the box. For our investigation we used two Low & Lou force-free field solutions. We present an entire analysis for one solution and for the second solution we test only the case where the input magnetogram is perturbed by noise.

3.1. Testing the method with analytical field 1

For the first semi-analytical force-free field solution of Low and Lou, we selected a depth of $l = 0.3$ times the edge length of the computational box, a tilt angle of $\Phi = 0.6 \cdot \pi/4$ deg, and a multipole order $n = 1$. In Fig. 1 we show the three components, B_x , B_y , B_z , of the magnetic field of Low & Lou of our choice of parameters. Our computational box has $64 \times 64 \times 32$ pixels.

We generated a discrete reference field as the solution of the conventional NLFFF problem with the boundary data from the Low and Lou. This field is close but not identical to the analytic

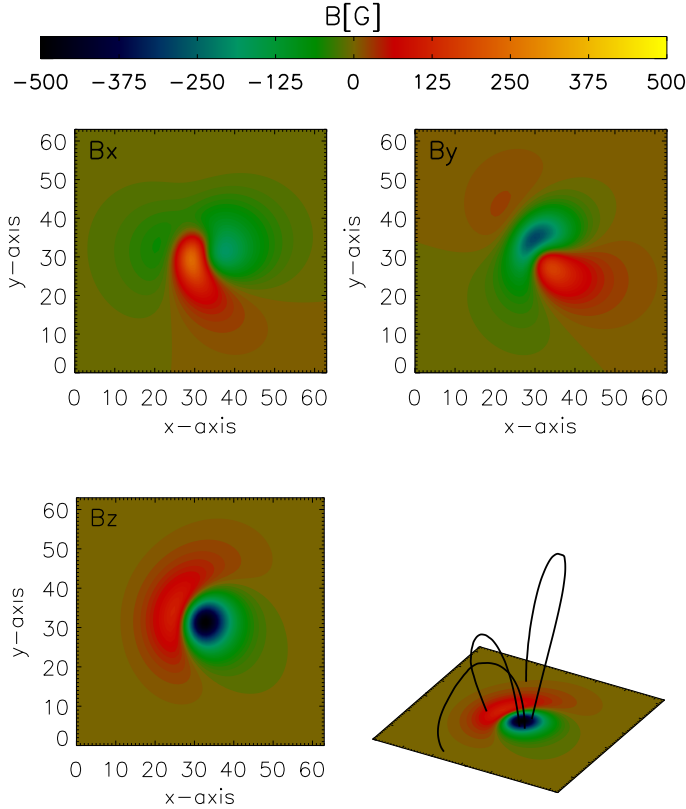


Fig. 1. Three Cartesian components of the synthetic magnetogram of Low & Lou used as bottom boundary in the $64 \times 64 \times 32$ pixel computational box. The top row shows the B_x (left) and B_y (right) components, the bottom row the B_z (left) component and an oblique view on the B_z magnetogram with the three loops extracted for our tests (right).

field of Low and Lou. From this discrete reference field, we generated three loops with a fourth-order Runge-Kutta method. These loops, termed consistent loops, were used as the source for the loop data used in our new variational term.

We made sure that we recovered the reference solution from the new S-NLFFF code if we used the correct surface boundary data of the reference field and the consistent loops in the term L_4 . This test essentially proves that our discretization is consistent. The angle between the loop tangents and the field of the reference solution should be zero. Because of the numerical roundoff errors mainly from the loop tracing, the actual angles we recover have an average of less than one degree and a maximum value of 2.8 deg. We considered this maximum angle as our standard angle error, which yields the upper bound for the deviation with which we can determine the alignment of the field and the loops.

When we apply our code to measured data, we cannot hope that boundary and loop data are consistent. We therefore performed two additional tests to demonstrate that our code can help to improve the results obtained with conventional extrapolation calculations.

- 1) Reconstructing the solution of Low and Lou in the case when the bottom surface data and the loop data are not consistent.
- 2) Reconstructing the solution of Low and Lou in the case when the loop data are consistent but the bottom surface data are contaminated by noise.

For both tests, we tried to determine the optimum regularization parameter ξ_4 of our new term. The relative magnitude of

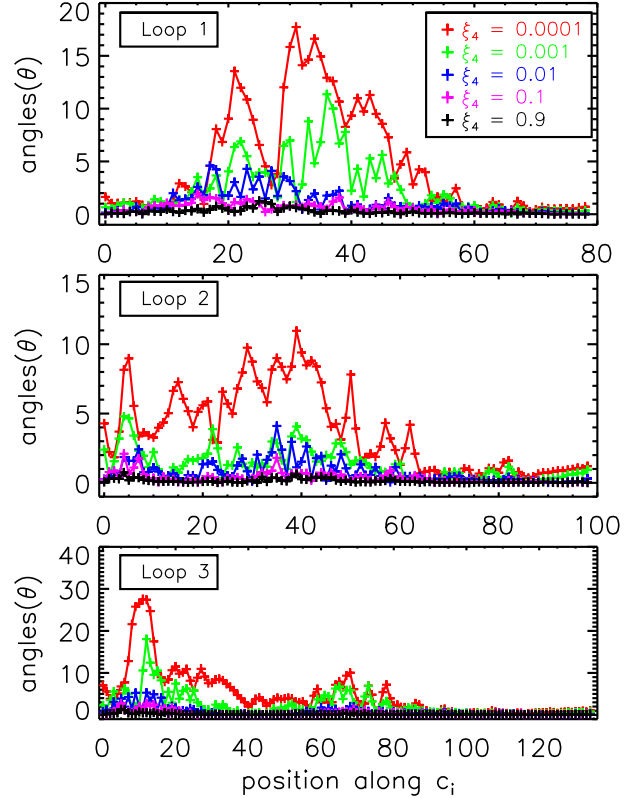


Fig. 2. Angles $\theta_i(s_j)$ between the tangent of the modified loops $i = 1, 2, 3$ and the interpolated magnetic field $\mathbf{B}(c_i(s_j))$ at curve parameter s_j along the loop. The different colors represent the angles for magnetic field models obtained with different regularization parameters $\xi_4 = 0.9$ (black), 0.1 (cyan), 0.01 (blue), 0.001 (green) and 0.0001 (red). The abscissa just counts the number of grid points along the loop.

the other regularization parameters has been determined before (Wiegelmann 2004) and was not changed.

3.1.1. Inconsistent surface and loop data

In this test, we modified the consistent loop coordinates by multiplying the z components of c_i with 1.05. Because of this manipulation, the angles between the consistent loops and the modified loops at the same loop parameter deviate by up to 20 deg.

These modified loops do not fit the boundary data anymore, and there is very probably no force-free magnetic field that can exactly satisfy both input data. Under these conditions, not all terms L_i^∞ can be iterated to low values. Moreover, if the z components of a magnetic field are enhanced in a similar way, the resulting field is not divergence-free anymore. It is therefore probable that a magnetic field that fits the three modified loops differs considerably from the reference field.

In Fig. 2 we display for various values of ξ_4 the angles $\theta_i(s_j)$ between the loop tangent $t_i(s_j)$ of the modified loop input data and the magnetic field \mathbf{B} returned from the S-NLFFF code and interpolated to $c_i(s_j)$.

Note that for $\xi_4 = 0$, we ran the conventional NLFFF code and obtained the reference field as a result. In this case, the angles $\theta_i(s_j)$ just represent the amount of modification applied to obtain the modified loops. With ξ_4 increasing, we forced the returned field to become increasingly aligned with the modified loops so that $\theta_i(s_j)$ decreases. The angles varied significantly along the loop and differently for different loops. With ξ_4 near

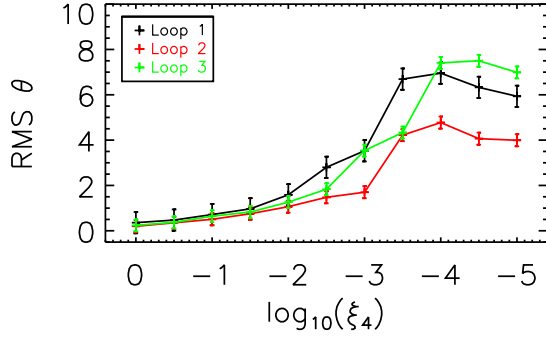


Fig. 3. Dependence of the root mean square angle θ with ξ_4 for each modified loop as shown in Fig. 2.

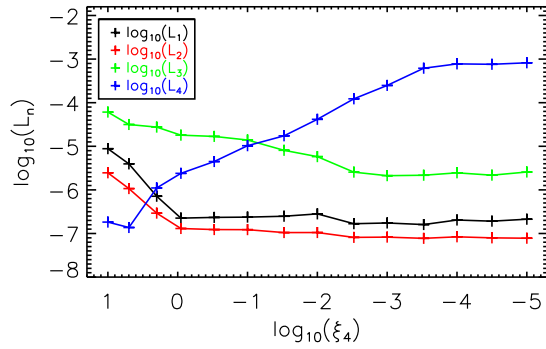


Fig. 4. Dependence of $\log \mathcal{L}_1^\infty$ (black), $\log \mathcal{L}_2^\infty$ (red), $\log \mathcal{L}_3^\infty$ (green) and $\log \mathcal{L}_4^\infty$ (blue) on $\log \xi_4$ for correct bottom data and modified loop data.

Table 1. Dependence of \mathcal{L}_1^∞ , \mathcal{L}_2^∞ , \mathcal{L}_3^∞ and \mathcal{L}_4^∞ on ξ_4 for the analytical field 1.

ξ_4	\mathcal{L}_1^∞	\mathcal{L}_2^∞	\mathcal{L}_3^∞	\mathcal{L}_4^∞	$\mathcal{L}_{\text{tot}}^\infty$
10.00000	2.4047	0.4909	0.3055	0.00001	3.2011
5.00000	0.6592	0.1632	0.1756	0.00007	0.9982
2.00000	0.0904	0.0408	0.1947	0.00065	0.3266
0.90000	0.0295	0.0170	0.0736	0.00075	0.1210
0.30000	0.0306	0.0161	0.0689	0.00140	0.1171
0.10000	0.0311	0.0160	0.0569	0.00323	0.1073
0.03000	0.0325	0.0137	0.0331	0.00544	0.0848
0.01000	0.0368	0.0137	0.0237	0.01301	0.0873
0.00300	0.0219	0.0106	0.0104	0.03837	0.0814
0.00100	0.0228	0.0108	0.0086	0.07791	0.1202
0.00030	0.0210	0.0101	0.0088	0.19312	0.2331
0.00010	0.0267	0.0109	0.0100	0.24288	0.2906
0.00003	0.0251	0.0104	0.0089	0.23786	0.2822
0.00001	0.0278	0.0102	0.0105	0.25723	0.3058
0.00000	0.0279	0.0103	0.0107	0.21720	0.0490

unity, we reduced the average angles for all loops to well below one degree. For the $\xi_4 = 0.90$ the maximum angle is 1.24 deg for loop 1, 0.75 deg for loop 2, and 1.34 deg for loop 3. To demonstrate the dependence of the angles θ_i with the regularization parameter, we also show the root mean square angle for each loop in Fig. 3. The error bars have the size of the standard angle error determined above.

This behavior is well reflected in the dependence of \mathcal{L}_4^∞ on the regularization parameter ξ_4 shown in Table 1 and Fig. 4 along with the variation of the other terms \mathcal{L}_i^∞ . Again, $\xi_4 = 0$ represents the reference field solution, and the values of \mathcal{L}_i^∞ in this case can serve as reference values that can be achieved with the discretization we chose. As expected from the improved angles $\theta_i(s_j)$, the term \mathcal{L}_4^∞ decreases with increasing ξ_4 .

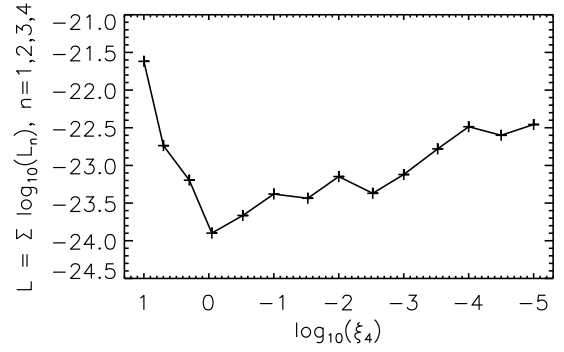


Fig. 5. Dependence of $\sum_i \log \mathcal{L}_i^\infty$ on $\log \xi_4$ for correct bottom data and modified loop data. The position of the minimum is assumed to yield the best-fit value for ξ_4 .

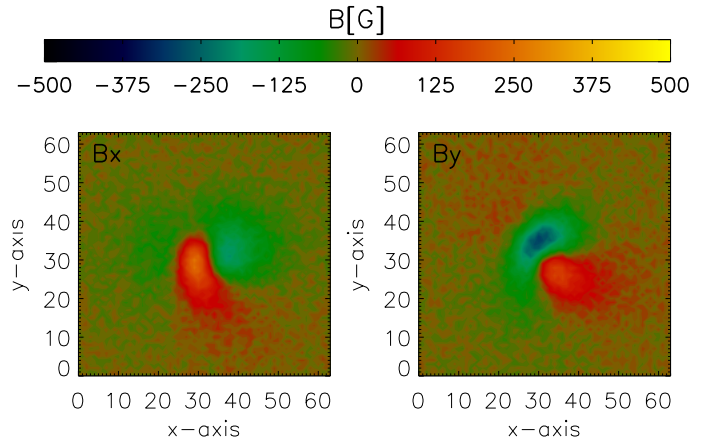


Fig. 6. Horizontal components of the magnetogram Low & Lou modified by adding noise. The vertical component is unchanged as in Fig. 1.

However, the better we fit the loop data, the stronger the discrepancy with the surface data, as reflected in \mathcal{L}_3^∞ and for high values $\xi_4 > 1$ also with the force-free and divergence-free conditions in \mathcal{L}_1^∞ and \mathcal{L}_2^∞ . Hence with the choice of ξ_4 , we can shift the emphasis between the boundary magnetogram and the loop data if they are inconsistent. If ξ_4 is smaller than unity, we obtain a nearly force-free magnetic field as proven by the only small variations of \mathcal{L}_1^∞ and \mathcal{L}_2^∞ with ξ_4 in this range. For values $\xi_4 > 1$, the values of \mathcal{L}_1^∞ and \mathcal{L}_2^∞ rise indicating that the field model increasingly deviates from a force-free and divergence-free solution. The best-fit value of ξ_4 that minimizes $\sum \log \mathcal{L}_i$ therefore lies near unity. In Fig. 5 we show the dependence of $\sum \log \mathcal{L}_i$ from $\log \xi_4$.

3.1.2. Noisy surface data

In this test we used the consistent loop data as input, but we modify the boundary data by random noise. A force-free field cannot be found for every boundary condition, and by adding noise to the boundary data, it very probably becomes inconsistent with a force-free field above, even if we do not constrain the problem further by additional loop data. The aim of the test is to show that adding the loop data improves the field model we compute in the end.

In Fig. 6 we show the modified boundary data. The noise is added to the B_x and B_y components of the magnetic field and amounts to about 3% of the maximum absolute values in the respective component. B_z is left unchanged because the horizontal

Table 2. Dependence of VC , CS , E_m and E_n on ξ_4 for the analytical field 1.

ξ_4	VC	CS	E_m	E_n
10.0000	0.9614	0.8981	0.3521	0.3598
5.00000	0.9647	0.9039	0.3392	0.3502
2.00000	0.9724	0.9153	0.3035	0.3286
0.90000	0.9844	0.9369	0.2321	0.2654
0.30000	0.9842	0.9351	0.2348	0.2699
0.10000	0.9842	0.9354	0.2348	0.2788
0.03000	0.9838	0.9348	0.2373	0.2713
0.01000	0.9836	0.9352	0.2382	0.2705
0.00300	0.9838	0.9342	0.2382	0.2735
0.00100	0.9834	0.9349	0.2389	0.2698
0.00030	0.9837	0.9345	0.2373	0.2698
0.00010	0.9835	0.9327	0.2400	0.2748
0.00003	0.9835	0.9323	0.2403	0.2761
0.00001	0.9833	0.9322	0.2412	0.2765
0.00000	0.9833	0.9319	0.2416	0.2775

(or plane of the sky) components are typically much less precise than the vertical (or line of sight) component.

We applied these input data to the S-NLFFF code as above and again varied ξ_4 over a wide range of values. Again we were able to successfully force the field model to become aligned with the loop data if we increased ξ_4 to unity.

In Table 2 we present commonly used figures of merit. The columns list the vector correlation (VC), the Cauchy-Schwartz (CS) product, the normalized vector error (E_n), and the mean vector error (E_m) defined as follows (Schrijver et al. 2006):

$$VC = \frac{\sum_i \tilde{\mathbf{B}}_i(\xi_4) \cdot \mathbf{b}_i}{\left(\sum_i |\tilde{\mathbf{B}}_i(\xi_4)|^2 \sum_i |\mathbf{b}_i|^2\right)^{1/2}} \quad (9)$$

$$CS \equiv \frac{1}{N} \sum_i \frac{\tilde{\mathbf{B}}_i(\xi_4) \cdot \mathbf{b}_i}{|\tilde{\mathbf{B}}_i(\xi_4)| |\mathbf{b}_i|} \equiv \frac{1}{N} \sum_i \cos \gamma_i \quad (10)$$

$$E_n = \frac{\sum_i |\mathbf{b}_i - \tilde{\mathbf{B}}_i(\xi_4)|}{\sum_i |\tilde{\mathbf{B}}_i(\xi_4)|} \quad (11)$$

$$E_m = \frac{1}{N} \sum_i \frac{|\mathbf{b}_i - \tilde{\mathbf{B}}_i(\xi_4)|}{|\tilde{\mathbf{B}}_i(\xi_4)|} \quad (12)$$

Here \mathbf{b} is the NLFFF field model when the solution of Low and Lou was used as magnetogram input, $\tilde{\mathbf{B}}(\xi_4)$ is the S-NLFFF field model, when the magnetogram of Low and Lou perturbed by noise was used. Here, i sums over the N grid points in the computational domain. A value of unity for VC and CS means that the fields are identical or parallel, respectively. For E_n and E_m a value equal to zero means that the two vector fields agree perfectly.

In Fig. 7 the root mean square angle is shown between the loop tangents and the local magnetic field $\tilde{\mathbf{B}}$ interpolated at the respective position $\mathbf{c}_i(s_j)$.

For the best-fit value $\xi_4 = 0.9$ of the regularization parameter, the root mean square angle is well below 1 deg. The maximum absolute deviation of the local field from the loop tangent is 2.1 deg, which is on the order of the standard angle error introduced above. These norms also include angles close to the foot points where the field if extrapolated without the loop data, that is, for $\xi_4 = 10^{-5}$, is varying heavily because of the influence of the noisy boundary data. Therefore the root mean square angle for $\xi_4 \leq 10^{-3}$ in Fig. 7 is strongly enhanced. The field extrapolated from the noisy boundary data makes in this case

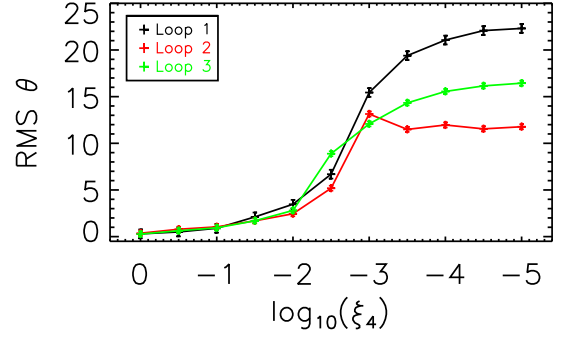


Fig. 7. Dependence of the root mean square of the angles θ between the loop tangent and the local field direction along each of the three consistent loops on ξ_4 .

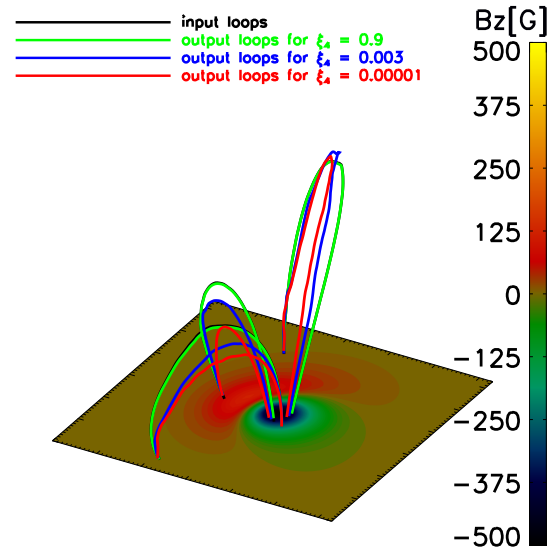


Fig. 8. Oblique view of the B_z magnetogram with the plot of the initial loops (black, hidden behind the almost identical green loops) used as input data and of output loops for $\xi_4 = 0.9$ (green), for $\xi_4 = 0.003$ (blue) and for $\xi_4 = 0.00001$ (red).

an average angle of up to 20 deg with the consistent loop direction. The loops for three values of ξ_4 are displayed in Fig. 8. These loops are traced in the same manner as the initial loop (the black curve from Fig. 8), starting from the same foot points as the initial loop. As expected from the deviation angles in Fig. 7, the loops traced from the extrapolated field approach the input data as ξ_4 approaches unity until they become indistinguishable at $\xi_4 = 0.9$. In Figs. 9 and 10, we display the dependence of the terms \mathcal{L}_i^∞ on ξ_4 . Probably as a result of the influence of the boundary noise in the regions not accessed by the three loops, the extrapolated field there has steeper gradients than the standard field, so that the terms \mathcal{L}_1^∞ and \mathcal{L}_2^∞ , which measure how far the field is force- and divergence-free, are about a factor 7–10 higher than for the noiseless reference field. These values hardly depend on ξ_4 as long as $\xi_4 \leq 1$ probably because the region influenced by the loops is smaller than the total computational volume. Definitely, for the different ξ_4 values chosen (Fig. 9), different field solutions were produced (see Fig. 8). Their variation, however, has little effect on the terms \mathcal{L}_1^∞ , \mathcal{L}_2^∞ , and \mathcal{L}_3^∞ . This shows that small changes in the magnetogram boundary comply with force-free fields that produce different field lines at some distance from the surface. This insensitivity is only constrained by the new term \mathcal{L}_4^∞ , as shown by its variation in Fig. 9.

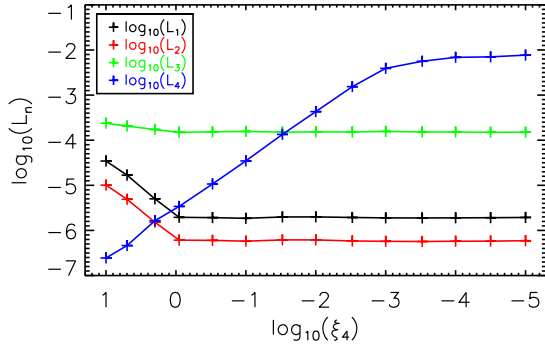


Fig. 9. Dependence of $\log \mathbb{L}_1^\infty$ (black), $\log \mathbb{L}_2^\infty$ (red), $\log \mathbb{L}_3^\infty$ (green) and $\log \mathbb{L}_4^\infty$ (blue) on $\log \xi_4$ for noisy bottom data and consistent loop data.

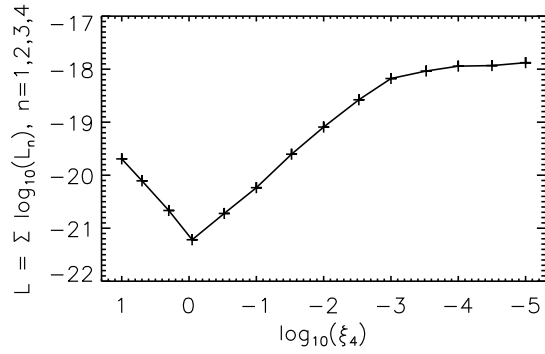


Fig. 10. Dependence of $\sum_i \log \mathbb{L}_i^\infty$ on $\log \xi_4$ for noisy bottom data and consistent loop data. The position of the minimum is assumed to yield the best-fit value for ξ_4 .

The boundary data term \mathbb{L}_3^∞ likewise hardly depends on ξ_4 in this particular test because the noise level chosen here is high, and even with $\xi_4 = 0$, a force-free magnetic field cannot be fitted to the boundary data to cause $\log \mathbb{L}_3^\infty$ to drop below about -0.2 . However, as expressed already by the root mean square angle, we can effectively align the field along the loop depending on how strong we shift the emphasis onto the loop term \mathbb{L}_4 by varying ξ_4 . The best-fit ξ_4 is again close to unity.

3.2. Testing the method with analytical field 2

For the second semi-analytical force-free field solution of Low and Lou, we selected a depth of $l = 0.3$ times the edge length of the computational box, a tilt angle of $\Phi = 4 \cdot \pi/5$ degrees for the polar axis and a multipole order $n = 3$. This is the same configuration as was used as a test in Schrijver et al. (2006). For this case, the computational box has $64 \times 64 \times 32$ pixels. Here, we only performed the test for the case when solution is perturbed by noise. We applied random noise to the boundary data in the same manner as for analytical field 1. The noisy boundary data together with the consistent loops were used as input to the S-NLFFF code for different ξ_4 values.

In Table 3 we display the output values of the force-free term (\mathbb{L}_1^∞), the divergence free term (\mathbb{L}_2^∞), the lower boundary term (\mathbb{L}_3^∞) and the loop term (\mathbb{L}_4^∞). The quality of the extrapolation $\tilde{\mathbf{B}}(\xi_4)$ is again measured by the figures of merit (9)–(11) where as reference we used field \mathbf{b} . The obtained values of the four terms (VC , CS , E_m , E_n) as a function of ξ_4 are presented in Table 4. For $\xi_4 = 0.9$ we again obtain the best solutions for these metrics.

Table 3. Dependence of \mathbb{L}_1^∞ , \mathbb{L}_2^∞ , \mathbb{L}_3^∞ and \mathbb{L}_4^∞ on each ξ_4 for analytical field 2.

ξ_4	\mathbb{L}_1^∞	\mathbb{L}_2^∞	\mathbb{L}_3^∞	\mathbb{L}_4^∞
0.90000	0.3401	0.1441	1.6179	0.0280
0.10000	0.3467	0.1463	1.5077	0.1918
0.01000	0.3582	0.1564	0.5180	1.2977
0.00100	0.3456	0.1538	0.4874	8.3740
0.00010	0.3430	0.1599	1.5189	16.4119
0.00001	0.3581	0.1654	1.4978	19.5104
0.00000	0.3518	0.1637	1.4976	0.00000

Table 4. Dependence of VC , CS , E_m and E_n on each ξ_4 for the analytical field 2.

ξ_4	VC	CS	E_m	E_n
0.90000	0.9907	0.8512	0.2920	0.5224
0.10000	0.9884	0.8297	0.3253	0.5875
0.01000	0.9876	0.8338	0.3324	0.5762
0.00100	0.9872	0.8305	0.3527	0.6132
0.00010	0.9877	0.8386	0.3463	0.5901
0.00001	0.9876	0.8358	0.3505	0.6009

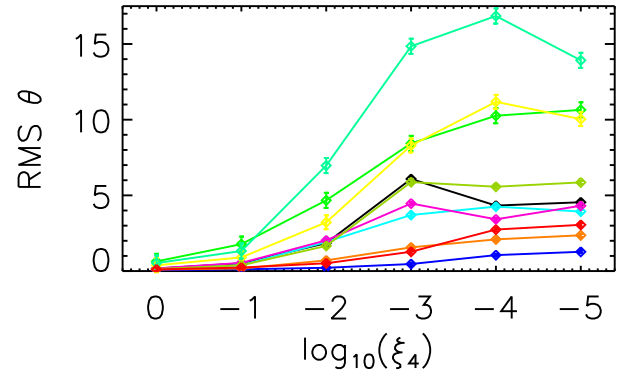


Fig. 11. Dependence of the root mean square of the angles θ between the loop tangent and the local field direction along each of the ten consistent loops on ξ_4 . For each loop, a different color code has been used.

As for the above tests, the angle between the loop tangents and the extrapolated magnetic field decrease as the fit parameters ξ_4 increase. Figure 11 shows the root mean square of the angles (θ_i) with $\log \xi_4$ for each of the ten loops used as input.

Finally, we checked whether the new term can help to improve the magnetic field model beyond what we can achieve with noisy boundary data alone. We defined three different subvolumes inside the computational box (SV_1 , SV_2 , SV_3). SV_1 is the union of the smallest possible quadrilateral boxes around each loop with edges in x , y , z direction. SV_2 and SV_3 comprises the same boxes centered around each loop with edge lengths enhanced by a factor 1.25 and 1.5, respectively.

In Fig. 12, we display the average error (Eq. (13)) for the three subvolumes of the extrapolated field with our new code with respect to the reference field for different values of ξ_4 . The reference field here is the extrapolation for ideal boundary data unperturbed by noise. For this case, $\xi_4 = 0$ because the loop data are unnecessary for ideal boundary data.

$$\langle \delta B \rangle = \langle \tilde{\mathbf{B}}(\xi_4) - \mathbf{b} \rangle \quad (13)$$

where $\tilde{\mathbf{B}}(\xi_4)$ is the magnetic field output obtained from the S-NLFFF extrapolation code, which uses the noisy magnetogram and the correct loops as input.

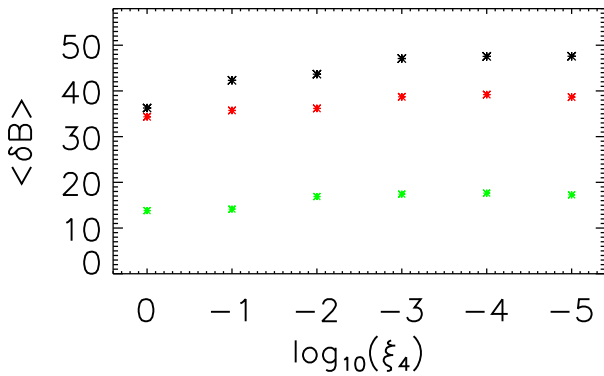


Fig. 12. Average vector difference between the S-NLFFF and NLFFF output magnetic field on $\log \xi_4$. Black asterisk represents the calculated $\langle \delta B \rangle$ for subvolume SV_1 , red asterisk the calculated $\langle \delta B \rangle$ for subvolume SV_2 and green asterisk the calculated $\langle \delta B \rangle$ for subvolume SV_3 .

Even though we used ten loops, the improvement of the field model by the new term is relatively weak for the best-fit value of $\xi_4 = 0.9$. The smallest subvolume (SV_1) only accounts for 0.26% of the total computational box.

4. Conclusions

We have proposed a new algorithm to improve the magnetic field model obtained from the force-free field extrapolation of magnetogram data. The new feature of the procedure is to incorporate the information of field-aligned loops obtained from EUV image pairs and processed by stereoscopy to 3D curves to approximate the shape of coronal loops.

If the magnetogram data are exact and the loop data are consistent, we find that the algorithm produces the unique solution as expected. In this theoretical case, the correct solution is also obtained even if the loop data are omitted. In most practical cases, however, it cannot be expected that the magnetogram data or the loop reconstruction are without errors. We have tested situations in which the two data sets were not entirely consistent. We found that for realistic error amplitudes we can achieve a good alignment of the magnetic model field with the loop curves without deteriorating the level of force-freeness. If these errors are present, a whole set of force-free fields is possible as solution with slightly different fields at the lower boundary that deviate from the magnetogram data within a typical measurement error. In these cases the additional loop information constrains the solution effectively, and from all possible solutions, we obtain the one that is best aligned with the imposed loop shapes.

The conclusion that noisy data allow multiple solutions if small deviations are allowed between the magnetogram data and the lower boundary of the model field can also be drawn from the results reported by De Rosa et al. (2009). All NLFFF codes produced model fields that closely matched the observed magnetogram data, but they were mutually different at higher altitudes and differed from the 3D loop shapes derived from stereoscopy. We attribute this deficiency to the poorly conditioned of the boundary value problem: little noise in the magnetogram data may cause changes in the solution especially at larger distances from the surface. From our tests, this is demonstrated by

the fact that we can modify the solution within some bounds by choosing different values for the regularization parameter ξ_4 without much affecting the force-freeness, divergence-freeness or the boundary data error. The new variational term we introduced makes use of this freedom to align the model field with the loop shapes.

Using the regularization parameter ξ_4 , we can allow either the magnetogram or the loop data to gain more influence on the final solution without significantly affecting the vanishing of the divergence or the Lorentz force. If both data terms are properly normalized by their measurement error, $\xi_4 \simeq 1$ is the best-fit value. In the cases we tested, the angles of the local field to the field line direction were then reduced to less than a degree on average.

Our algorithm still has to be applied to real data. An investigation of this kind is under way. Provided that all the data are available, we are confident that we will be able to produce a more reliable force-free magnetic field model for the corona than with conventional tools. In many cases, a vector magnetogram and two simultaneous STEREO images are not available. We therefore intend to modify our code to also cope with the case when the field extrapolation is constrained by a loop projection from only one EUV image.

Acknowledgements. I.C. acknowledges a Ph.D. fellowship from the International Max Planck Research School on Physical Processes in the Solar System and Beyond. The work of T.W. was supported by DLR fund 50 OC 1301.

References

- Amari, T., Boulmezaoud, T. Z., & Aly, J. J. 2006, *A&A*, 446, 691
- Arnaud, J. 1992, in *Coronal Streamers, Coronal Loops, and Coronal and Solar Wind Composition*, ed. C. Mattok, *ESA SP*, 348, 285
- Aschwanden, M. J. 2011, *Liv. Rev. Sol. Phys.*, 8, 5
- Aschwanden, M. J. 2013, *Sol. Phys.*, 287, 323
- Aschwanden, M. J., & Malanushenko, A. 2013, *Sol. Phys.*, 287, 345
- Aschwanden, M. J., Wuelser, J.-P., Nitta, N. V., et al. 2012, *ApJ*, 756, 124
- Carcedo, L., Brown, D. S., Hood, A. W., Neukirch, T., & Wiegmann, T. 2003, *Sol. Phys.*, 218, 29
- De Rosa, M. L., Schrijver, C. J., Barnes, G., et al. 2009, *ApJ*, 696, 1780
- Hansen, P. C. 2010, *Discrete inverse problems insight and algorithms* (Philadelphia: Society for Industrial and Applied Mathematics)
- House, L. L., Querfeld, C. W., & Rees, D. E. 1982, *ApJ*, 255, 753
- Inhester, B. 2006 [[arXiv:astro-ph/0612649](https://arxiv.org/abs/astro-ph/0612649)]
- Inhester, B., & Wiegmann, T. 2006, *Sol. Phys.*, 235, 201
- Leka, K. D., Barnes, G., Crouch, A. D., et al. 2009, *Sol. Phys.*, 260, 83
- Lin, H., & Penn, M. J. S. T. 2000, *ApJ*, 541, L83
- Low, B. C., & Lou, Y. Q. 1990, *ApJ*, 352, 343
- Metcalf, T. R., Jiao, L., McClymont, A. N., Canfield, R. C., & Uitenbroek, H. 1995, *ApJ*, 439, 474
- Metcalf, T. R., Leka, K. D., Barnes, G., et al. 2006, *Sol. Phys.*, 237, 267
- Moon, Y.-J., Choe, G. S., Yun, H. S., Park, Y. D., & Mickey, D. L. 2002, *ApJ*, 568, 422
- Régnier, S. 2013, *Sol. Phys.*, 288, 481
- Schrijver, C. J., De Rosa, M. L., Metcalf, T. R., et al. 2006, *Sol. Phys.*, 235, 161
- Tadesse, T., Wiegmann, T., Inhester, B., & Pevtsov, A. 2011, *A&A*, 527, A30
- Thalmann, J. K., Inhester, B., & Wiegmann, T. 2011, *Sol. Phys.*, 272, 243
- Valori, G., Kliem, B., & Fuhrmann, M. 2007, *Sol. Phys.*, 245, 263
- Wheatland, M. S., Sturrock, P. A., & Roumeliotis, G. 2000, *ApJ*, 540, 1150
- Wiegmann, T. 2004, *Sol. Phys.*, 219, 87
- Wiegmann, T., & Inhester, B. 2010, *A&A*, 516, A107
- Wiegmann, T., & Neukirch, T. 2002, *Sol. Phys.*, 208, 233
- Wiegmann, T., & Sakurai, T. 2012, *Liv. Rev. Sol. Phys.*, 9, 5